UC Irvine
UC Irvine Previously Published Works

Title

Surface-enhanced coherent anti-Stokes Raman scattering of molecules near metal-dielectric nanojunctions.

Permalink

https://escholarship.org/uc/item/6jf327c9

Journal

Journal of Physical Chemistry C, 126(20)

ISSN

1932-7447

Authors

Abedin, Shamsul
Roy, Khokan
Jin, Xin
et al.

Publication Date

2022-05-26

DOI

10.1021/acs.jpcc.2c01642

Peer reviewed

Surface-enhanced coherent anti-Stokes Raman scattering of molecules near metal-dielectric nanojunctions

Shamsul Abedin[†], Khokan Roy[‡], Xin Jin[¶], Hui Xia[¶], S. R. J. Brueck[¶], Eric O. Potma[‡]

[†]Department of Chemical and Biomolecular Engineering, University of California, Irvine, CA 92697, USA

[‡]Department of Chemistry, University of California, Irvine, CA 92697, USA

[¶]Armonica Technologies, Inc., Albuquerque, NM 87110, USA

Abstract

We discuss an experimental configuration consisting of {Au film}-molecule-{Au particle} or {Au film}-molecule-{Si particle} nanojunctions for performing wide-field surface-enhanced CARS (SE-CARS) measurements in a reproducible and controllable manner. While the allowable illumination dosage in the {Au film}-molecule-{Au particle} case is limited by the strong two-photon background from the gold, we successfully generate a detectable coherent Raman response from a molecular monolayer using the lowest reported average power densities to-date. With a vision to minimize the two-photon background and the intrinsic losses observed in all-metal plasmonic systems, we examine the possibility of using high-index dielectric particles on top of a thin metal film to generate strong nanoscopic hotspots. We demonstrate repeatable SE-CARS measurements at the {Au film}-molecule-{Si particle} heterojunction, underlining the usability of this experimental geometry. This work paves the way for the development of next-generation of chemical and biomolecular sensing assays that can minimize some of the major drawbacks encountered in fragile and lossy all-metal plasmonic systems.

Graphical Abstract

epotma@uci.edu .
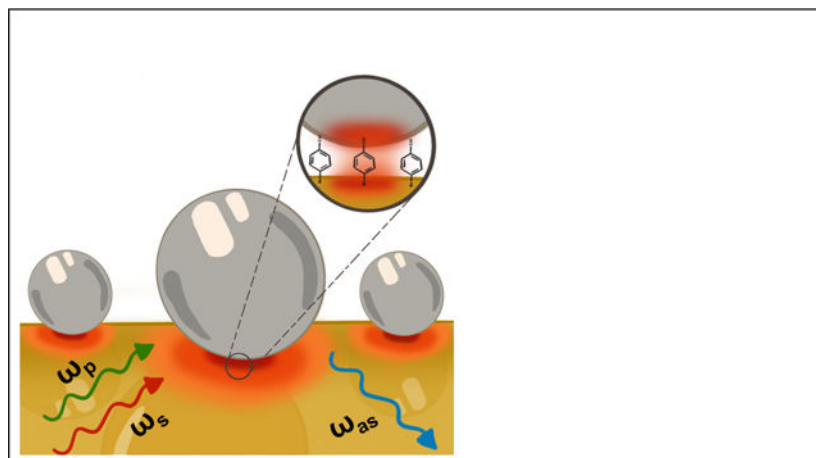
Introduction

Surface enhanced Ramans scattering (SERS) is a widely used spectroscopic tool for sensing molecules at low concentrations. In SERS, plasmonic nano-antenna systems enhance the sensitivity of the otherwise weak Raman effect.[1–3] These metallic nanostructures support surface plasmon resonances that can confine propagating electromagnetic radiation to nanoscale regions, where the molecule of interest is efficiently driven. Subsequently, the antenna enhances the radiation of the induced Raman polarization, enabling strong signal collection in the far-field.[4–8] The enhancement mechanism of SERS is well understood, and well-designed nanostructures have successfully pushed the sensitivity of this technique to the single-molecule limit.[9–11] While SERS does allow massive enhancement of the feeble Raman effect, it is limited in terms of acquisition rates and struggles to record spectra at rates faster than ~ 10 Hz in the single molecule limit. For single molecule applications that require much faster readout rates, such as DNA sequencing applications,[12,13] the SERS mechanism alone may not be sufficient.

In coherent Raman scattering (CRS) the vibrational transition in the molecule is stimulated, and thus the molecular transition rate can be significantly higher compared to the transition rate in spontaneous Raman scattering. In addition, in the case of an ensemble of molecules, the molecular oscillators are driven in unison, producing coherent radiation that takes advantage of the constructive interference between the dipolar radiators. The combination of these two effects can give rise to much higher signal levels in CRS compared to linear Raman methods. For this reason, CRS spectroscopy and microscopy techniques have gained popularity in applications where the long signal acquisition time of spontaneous Raman scattering is a limiting factor.[14–19] Various CRS implementations have demonstrated spectral acquisition rates that are many orders of magnitude faster than what can be achieved with spontaneous Raman or SERS. Examples include Fourier transform coherent anti-Stokes Raman scattering (CARS) with spectral acquisition rates of 100 kHz[20,21] and arrayed detection of stimulated Raman scattering (SRS) at spectral acquisition rates of 200 kHz.[22]

Such fast spectral acquisition rates, however, were obtained for relatively high molecular concentrations, and are thus not easily extended to the limit of a few molecules. In this

limit, the coherent amplification of the CRS signal no longer applies,[17] yet the stimulated vibrational transition afforded by the CRS process still offers a potential mechanism for enhanced transition rates relative to spontaneous Raman scattering. In this context, the combination of CRS with the field enhancement provided by surface plasmon resonances appears a route toward higher Raman radiation rates than those obtained in conventional SERS.

Surface-enhanced CRS was first demonstrated in the form of surface-enhanced CARS (SE-CARS) in 1979, using the propagating surface plasmon polariton (SPP) modes supported on a flat silver film to amplify the CARS spectrum of liquid benzene.[23] Subsequent work has focused predominantly on plasmonic junctions in gold and silver nano-structures, confirming the ability of plasmonic resonances to amplify the CRS signal, even reaching the single-molecule limit.[3,24–27] These metallic systems are chosen as they feature some of the highest achievable field-enhancement factors. However, there is a limit to how much incident radiation can be applied before photo-induced breakdown of the plasmonic substrate and the molecule occurs.[28–36] It has been shown that under ultrafast excitation, the electron temperature can reach thousands of Kelvin,[37] and that also the lattice temperature can go up, affecting the structural integrity of the junction. It has also been reported that near local peak intensities (defined as $\beta^2 I$, where β is the local field enhancement factor and I is the incident intensity) of $10^{12} – 10^{13}$ W/cm^2, bending of the potential followed by electron tunneling can cause photo-induced ionization of the molecule.[38] The heat-induced morphological distortions at the metallic junctions are accompanied by steep field gradients that defy standard Raman selection rules, and involvement of charge-transfer plasmons and plasmon-induced chemistry complicate matters, making these SE-CRS measurements extremely difficult to reproduce.[2] As a result, there is a need for new SE-CRS systems that enable reliable and reproducible measurements by substantially minimizing the inherent drawbacks of the metal-molecule-metal nanojunctions used for SE-CRS thus far.

Addressing this issue of reproducibility of SE-CRS measurements requires a reimagining of experimental geometries. Plasmonic systems that are easy to fabricate repeatably and that can efficiently produce a robust optical response with lower local heating can play an important role here. A case in point is the use of a flat gold film on a glass substrate as the main antenna system. We have previously shown that such a system provides reproducible total enhancement factors of ~ 10^6 for the case of SE-CARS.[39,40] Even higher enhancement factors can be expected for nanoantenna systems comprised of metal particles placed on top of a metal film. This particle-on-a-film configuration has been explored by multiple groups as a promising platform for reproducible (linear) spectroscopic studies.[41–45] Facile fabrication methods and high attainable field enhancement factors make this system particularly suitable for SERS studies.

While this particle-on-a-film geometry substantially mitigates heating issues, the thermal load at the junction can be further reduced by using high-index dielectric particles that are known to exhibit higher specific heat capacities while also showing excellent antenna properties. It has been recognized that Si and GaP dielectric particles provide strong field enhancements at optical and NIR frequencies while producing orders-of-magnitude lower dissipative losses compared similar structures made of gold.[46,47] The mechanism behind

metallic and dielectric nanoantenna induced field enhancement processes are fundamentally different. The metal induced plasmonic fields are generated as a result of free-electron plasma oscillations.[48] In dielectric nanoantennas, electromagnetic field localization arises due to the generation of strong displacement currents inside the material. These currents generate inner-electric field distributions, which are accompanied by electric fields outside the material as well. As a result, when dieletric particles form nanojunctions, they also provide field enhancement in the cavity.[46,49] These high-index dielectric nanoparticles provide a low-loss alternative to their metallic counterparts, which we explore in this study as a potential platform for reliable surface-enhanced CRS sensing.

In this work, we seek to overcome the aforementioned inherent limitations of unpredictable SE-CARS enhancement systems. We utilize a simple experimental geometry to perform repeatable and controllable wide-field SE-CARS measurements at Au film-Au particle and Au Film-Si particle nanojunctions. We demonstrate successful generation of detectable SE-CARS signals using the lowest reported average incident intensities to date using a metal-molecule-metal nanojunctions. We also successfully perform a first-of-its-kind SE-CARS measurements at the metal-dielectric heterojunction, opening up the possibility of next generation of surface-enhanced coherent Raman sensors that do not rely on fragile metallic nano cavities.

Materials and Methods

Sample Preparation

Gold sensing surfaces are prepared using a physical vapor deposition (PVD) process. A 45 nm thick Au film on top of a 2 nm thick Cr adhesion layer is evaporated on BK7 coverslips (Corning). Note that this Cr layer introduces attenuation of the surface plasmon wave as a result of the poor (nonmetallic) optical properties of Cr at near-infrared wavelengths, yet it is used here to enable better adhesion of the gold to the glass coverslip. The coverslips are thoroughly cleaned prior to deposition by sonicating them in EtOH/water and acetone/water baths. Freshly prepared gold films are functionalized by overnight incubation in 5 mM ethanolic solution of 4-(mercaptomethyl)benzonitrile (MMBN) obtained from Sigma-Aldrich. 40 nm gold nanoparticles (Sigma-Aldrich) and 60 nm Silicon nanoparticles (Meliorum Technologies) are used without further purification. The particles are drop cast on functionalized films prior to measurements. Scanning electron measurements reveal that the drop-casting procedure results in the formation of small isolated clusters of 1–10 nanoparticles on the gold surface.

Optical Setup

The optical setup is based on an inverted Olympus IX73 microscope frame. The system uses a light source that consists of a pulsed laser and a synchronously-pumped optical parametric oscillator (OPO). The laser source is a Nd:Vanadate oscillator (Pico-Train, High-Q) producing ~7 ps pulses at a center wavelength of 1064 nm and is used as the Stokes beam for the SE-CARS measurements. Figure 1 provides a schematic of the optical layout.

A portion of the laser beam is frequency-doubled and then used to synchronously pump the OPO (Levante Emerald, APE Berlin) to generate a tunable (720 – 980 nm) pump beam. Both the pump and Stokes beams are conditioned to produce linearly polarized and collimated beams with clean, transverse Gaussian profiles. The spatially and temporally overlapped beams are then separately focused with plano-convex lenses (f = 250 mm) onto the backfocal plane (BFP) of a 60×, 1.49 NA (APON60XOTIRF, Olympus) objective lens, producing collimated beams at the exit pupil of the objective lens for wide-field illumination of the sample. The beams are incident at their respective Kretschmann angles to excite SPP modes at the gold/nanoparticle interface. After interacting with the target molecule, the anti-Stokes scattered radiation is generated and the epi-directed signal is separated from the incident fields by a dichroic mirror (850 nm SWP, Semrock) and projected onto an EM-CCD camera (iXon3, Andor) after going through two bandpass filters (794/32 nm, Semrock). The expanded beams produce a field of view (FOV) of $105 \times 105 \ \mu m^2$. For the SE-CARS measurements at Au film-Au particle nanojunctions, the average incident powers at the sample in both beams are kept low (5–10 mW in pump and 5–15 mW in Stokes) to avoid saturation of the EM-CCD with two-photon excited fluorescence (TPEL) and the images are collected at 1 second/frame. These power levels correspond to power densities of 0.64–1.27 $\mu W/\mu m^2$ for the pump and 0.64 – 1.91 $\mu W/\mu m^2$ for the Stokes beam in the sample plane. In the Au film-Si particle heterojunctions, the field enhancements are lower compared to Au-Au nanojunctions. This necessitates higher power levels (up to 140 mW of average power in each beam or 17.92 $\mu W/\mu m^2$) and longer integration times (30 seconds/frame).

Numerical Simulations

Numerical simulations of the local electromagnetic fields are performed using the finite-difference time-domain (FDTD) method (Ansys Lumerical FDTD). The Palik library is used for dielectric function estimation for all the materials involved.[50] The 2 nm Cr layer is ignored in the simulations. For a given sample, an incidence angle sweep is performed to find the Kretschmann angle for efficient excitation of propagating surface-plasmon polariton modes. Using the maximum coupling angle, subsequent simulations are performed to calculate electromagnetic fields at the vicinity of the nanojunction. Fine meshing of 0.167 nm is used in all cases. Experimental values for the thickness of the film, diameter of the particles and the cavity length are used for these calculations.

Results

SE-CARS at Au film-Au particle nanojunction

We use a high numerical aperture microscope objective-based Kretschmann configuration to individually couple the freely propagating pump and Stokes beams to the SPP modes supported on the planar gold film. The SPP coupling angles for each of the beams can be found by monitoring the back-reflection from the film on the detector. Equivalently, TPEL from the gold film can be monitored to find this angle.[51] This luminescent background is attributed to the interband transitions in the gold film and the subsequent radiative recombination of electron-hole pairs.[52]

We first perform SE-CARS measurements on a Au particle-Au film nanoantenna system in the wide-field Kretschmann configuration. Our target is 4-(mercaptomethyl)benzonitrile (MMBN), which is present as a monolayer on the surface of the gold film. A 40 nm diameter gold particle is placed atop the molecular layer, as shown schematically in Figure 2(a). Using finite-difference time-domain (FDTD) calculations for this experimental configuration, we find that the combined effect of propagating SPPs from the gold film and the LSPR of the gold particles results in an effective field enhancement factor β_p of 108 at a pump wavelength of 909 nm. Similarly, we find $\beta_s = 96$ at the Stokes wavelength ($\lambda_s = 1064$ nm) and $\beta_{as} = 117$ for the anti-Stokes wavelength ($\lambda_{as} = 793$ nm). Figure 2(b) shows the hotspot formed between the particle and the gold film under SPP illumination conditions. The hotspot size is found to be ~5 nm in diameter. Using a surface coverage of 6 molecules/nm^2,[53–55] we estimate that there are ~120 molecules in each electromagnetic hotspot under these conditions.

In the experiment, the average incident powers of both beams are kept low (5–10 mW in pump and 5–15 mW in Stokes) to avoid saturation of the EM-CCD with TPEL. With the resulting power densities in the 1 $\mu W/\mu m^2$ range, these average excitation intensities to generate a detectable CARS signal are lower than reported in previous studies. The TPEL background is generated by the pump beam and can be independently determined by blocking the Stokes beam. In the following, we subtract the TPEL background signal to isolate the SE-CARS signal.

Figure 3 shows the SERS spectrum of the Au-MMBN-Au structure near the 1604 cm^{-1} resonance of the aromatic ring vibration. The Figure also shows two wide-field SE-CARS images, taken at an off-resonance energy of 1560 cm^{-1} and at the on-resonance energy of 1606 cm^{-1}. The image shows small clusters of gold nanoparticles on the Au film. The difference between the on and off-resonant settings is evident and repeatable, and is attributed to the vibrational resonant excitation of MMBN. For the particular image shown in Figure 3, we observe average molecular signal levels of ~160 photons/s. Since the number of Au particles in the cluster varies from spot to spot, the variability of the SE-CARS signal observed here is mainly due to the morphology and number of particles within a given diffraction-limited probing spot.

We note that $\beta^2 I$ in this case is 2.83×10^9 W/cm^2, which is at least 3 orders of magnitude smaller than the photo-damage threshold of gold. From this, we can infer that in principle higher effective local peak intensity can be applied to generate more SE-CARS signal. While the "hot" cavity does enable strong light-matter interactions, TPEL (~1850 photons/s as shown in Figure 3) from the film and the plasmonic gold nanoparticles establish a limit on the allowable incident power levels. After TPEL subtraction, the background visible in the off-resonant image at 1560 cm^{-1} can be attributed to the coherent four-wave mixing (FWM) background from the gold nanojunction. The electronic FWM background in this case is on average ~13% relative to the molecular vibrational signal.

Under the current excitation conditions, the SE-CARS signal is clearly observed, yet the signal shows variation over time. Blinking-type behavior can be observed for several hotspots on the 1–100 s timescales. In addition, the magnitude of the SE-CARS signal

gradually decays on a timescale of ~ 3 minutes under constant illumination. We attribute these observations to thermal effects at the Au-Au junction. These observations have motivated us to explore metal film-dielectric particle heterojunctions that are less susceptible to thermal effects and that exhibit lower metal-induced TPEL.

SE-CARS at Au film-Si particle heterojunction

Next, we examine the capability of heterojunctions consisting of a metallic gold film and dielectric silicon nanoparticle to generate vibrationally resonant SE-CARS signal from the MMBN molecule. Electromagnetic field calculations (FDTD) provides insight into how the particle size and coupling angles for the pump, Stokes and anti-Stokes frequencies affect the overall CARS enhancement factor. Figure 4 demonstrates that the coupling angle changes more dramatically for the anti-Stokes radiation compared to the longer wavelength pump and Stokes beams.

While the Kretschmann angle changes rapidly for the shorter wavelengths, the simulations show that they have little impact on the attainable overall CARS enhancement factors. Figure 5(a) shows numerically calculated enhanced local fields in the vicinity of the Au film-Si particle junction. For a heterojunction consisting of a 45 nm Au film and a 60 nm Si nanoparticle, we calculate a moderately high β_p of ~35 at the pump wavelength of 909 nm. Similar calculations were performed for the Stokes and anti-Stokes wavelengths. Given that SE-CARS signal scales as $\beta_p^4 \beta_s^2 \beta_{as}^2$, we expect the local fields to be strong enough to generate vibrational response from the aromatic ring mode even with the low illuminating power densities that are being used in our wide-field SE-CARS microscope. As shown Figure 5(b), the overall CARS enhancement factor is predicted to remain near 10^{12} for the particle sizes studied here.

In the heteorjunction experiments, the average power in each of the incident beams is varied between 100–140 mW, corresponding to intensities of 12.8–17.92 $\mu W/\mu m^2$. Further increase of illumination dosage is not feasible as they have been observed to result in photo-induced thermal damage to the Au film itself. Given that the lateral size of the field distribution is approximately the same as in the case for Au-Au junction, we estimate that a similar number of molecules (~120) are being probed for each film-particle hotspot.

Figure 6 shows the wide-field SE-CARS spectrum (green dots) in the 1560–1630 cm^{-1} window. The SE-CARS data is overlaid on top of the CARS spectrum of the bulk MMBN (blue trace) that is shown as a reference. Unlike the wide-field SE-CARS measurements, the CARS spectrum of bulk MMBN is obtained using tightly focused beams produced by a 1.49 NA microscope objective. The SE-CARS measurements are taken at 10 cm^{-1} steps with the 1604 cm^{-1} resonance as the vibrational mode of interest. We observe a spectral SE-CARS profile that roughly resembles the CARS spectrum of bulk MMBN. The spectral dependence provides strong evidence that the SE-CARS signal from the Si-Au junction resolves the vibrationally resonant response of MMBN. The SE-CARS images show clear contrast between on and off resonant settings. The SE-CARS spectrum appears red-shifted from the bulk CARS spectrum of MMBN. It is possible that interaction between the Si surface and the nitrile terminal group of MMBN leads a different charge distribution, which in turn can shift the resonance frequency of the mode.[56]

The average molecular SE-CARS signal in this experiment is found as ~235 photons/s (as shown in Figure 6). We observe TPEL background from the Au film in this configuration as well. However, due to the non-luminescent and non-plasmonic nature of the Si nanoparticles, this background signal does not overwhelm the far-field detector. The TPEL background (~550 photons/s as shown in Figure 6) is subtracted to obtain the SE-CARS response from the MMBN molecule in this configuration as well.

Besides the TPEL background, we also observe FWM background. Though always present, this FWM background is not observed to be as strong as the TPEL background and is found to be less than 5% relative to the molecular SE-CARS signal, i.e. significantly less compared to the FWM contribution in the Au-Au nanojunction. Unlike the gold nanojunction, the heterojunction appears stable. We do not observe blinking of the SE-CARS signal on the time scale of minutes, and the overall magnitude of the signal also remains constant on this time scale. From this observation we infer that thermal effects are less prominent in the heterojunction compared to the situation in the Au-Au junctions.

Discussion

In this work, we have used an experimental configuration to perform wide-field SE-CARS microscopy experiments in a repeatable and controllable manner, using low incident intensities. This chosen geometry consists of Raman-active molecules placed inside a cavity formed between a nanoparticle and a planar gold film, while the illuminating pump and Stokes beams arrive at their respective Kretschmann angles in order to excite propagating SPP modes. We have used both metallic and dielectric nanoparticles to form these junctions and have successfully driven Raman coherences in the sample. This technique shows that we do not need to exclusively rely on lossy metallic platforms to create confined nanoscopic hotspots, as our results show that dielectric materials can be involved in the formation of the confined local fields required for SE-CARS.

Here, we have used collimated pump and Stokes beams for wide-field illumination. Compared to traditional point-scanning CARS microscopes. This wide-field geometry allows for orders-of-magnitude lower average intensities incident on the sample. In the Au film-Au particle configuration, the field enhancement in the junction exceeds one hundred times ($\beta > 100$). While the intense local field enables stronger light-matter interaction, the accompanying TPEL background makes it difficult to achieve higher signal levels by raising the illumination dosage. There is also a coherent FWM contribution from the gold itself because of its strong $\chi^{(3)}$ response. However, in the Kretschmann illumination mode, the background FWM signal is much weaker than the incoherent TPEL background from the gold. This observation correlates well with previous work.[2,39,40] In addition, thermal effects are present as intermittent blinking of the signal points, accompanied by an overall decay of the signal.

In order to reduce local heating effects at the junction and the strong TPEL radiation from the gold, we have used silicon nanoparticles that exhibit a high refractive index in the visible and near-infrared spectral range. Nanostructures fabricated from silicon and other similar high-index dielectric materials are known to provide significant confinement

of the electric and magnetic fields, making them ideal candidates for optical nanoantenna applications. Silicon's ability to provide strong local fields along with its low-loss nature and thermal stability are features that led us to explore its use for SE-CARS.[46,47] Numerical simulations show a total enhancement of ~ 10^{12} in the case of Au film-Si particle system. Note that because of the ~ β^8 dependence of the SE-CARS signal such enhancements are substantial compared to what is commonly achieved for SERS measurements. Yet, the total enhancement factor obtained here is still relatively modest for a SE-CARS measurement.

The use of Si as a high-index dielectric material to form nanojunctions minimizes some of the major drawbacks encountered in typical all-metal nanoantennas. In particular, the unfavorable structural changes to antennas due to local heating is reduced here significantly (because of lower optical absorption and higher specific heat of Silicon[47,49]) as evidenced through reduced blinking and improved stability of the signal. Both TPEL and FWM backgrounds are present in this geometry as well, but due to the non-luminescent and non-plasmonic nature of dielectric Si nanoparticles (with radii much larger than the exciton radius), the TPEL background is significantly reduced in Au film-Si particle systems. However, the lower effective β requires higher illumination dosage and longer acquisitions times to be able to generate detectable SE-CARS signal. The continued illumination at higher power densities can eventually damage the flat Au film, limiting the allowable radiation dosage in this geometry as well. Nevertheless, this metal film-dielectric particle system allows more control over the measurements compared to the metal film-metal particle system. The inherent limitation of this geometry is the strong TPEL background that is always present even though it is reduced for the dielectric particle-metal film heterojunction by more than a factor of 3 relative to the all-metal nanojunction. The next logical step in this field would be to use all-dielectric nanoantenna systems that are not susceptible to intense thermal effects at the junctions and that can effectively eliminate the TPEL background.

Conclusions

We have demonstrated an experimental geometry to perform reliable, repeatable and controllable SE-CARS measurements at metal film-metal particle and metal film-dielectric particle nanojunctions. We successfully show generation of molecular SE-CARS signals using the lowest reported average illumination densities to date. We also show SE-CARS spectroscopy at metal film-dielectric particle heterojunctions, paving the way for development of new biomolecular sensing assays that do not rely on lossy and fragile metallic nanojunctions.

Acknowledgement

References

(1). McCreery RL Raman spectroscopy for chemical analysis; John Wiley & Sons, 2005; Vol. 225.

(2). Fast A; Potma EO Coherent Raman scattering with plasmonic antennas. Nanophotonics 2019, 8, 991–1021.

(3). Zong C; Premasiri R; Lin H; Huang Y; Zhang C; Yang C; Ren B; Ziegler LD; Cheng J-X Plasmon-enhanced stimulated Raman scattering microscopy with single-molecule detection sensitivity. Nature communications 2019, 10, 1–11.

(4). Fleischmann M; Hendra P; McQuillan A Raman spectra of pyridine adsorbed at a silver electrode. Chemical Physics Letters 1974, 26, 163 – 166.

(5). Jeanmaire DL; Duyne RPV Surface raman spectroelectrochemistry: Part I. Heterocyclic, aromatic, and aliphatic amines adsorbed on the anodized silver electrode. Journal of Electroanalytical Chemistry and Interfacial Electrochemistry 1977, 84, 1 – 20.

(6). Moskovits M Surface-enhanced spectroscopy. Rev. Mod. Phys 1985, 57, 783–826.

(7). Willets KA; Van Duyne RP Localized surface plasmon resonance spectroscopy and sensing. Annu. Rev. Phys. Chem 2007, 58, 267–297. [PubMed: 17067281]

(8). Zhang R; Zhang Y; Dong Z; Jiang S; Zhang C; Chen L; Zhang L; Liao Y; Aizpurua J; Luo Y. e. et al. Chemical mapping of a single molecule by plasmon-enhanced Raman scattering. Nature 2013, 498, 82–86. [PubMed: 23739426]

(9). Nie S; Emory SR Probing single molecules and single nanoparticles by surface-enhanced Raman scattering. science 1997, 275, 1102–1106. [PubMed: 9027306]

(10). Le Ru EC; Etchegoin PG Single-molecule surface-enhanced Raman spectroscopy. Annual review of physical chemistry 2012, 63, 65–87.

(11). Dieringer JA; Lettan RB; Scheidt KA; Van Duyne RP A Frequency Domain Existence Proof of Single-Molecule Surface-Enhanced Raman Spectroscopy. Journal of the American Chemical Society 2007, 129, 16249–16256. [PubMed: 18052068]

(12). Kneipp K; Kneipp H; Kartha VB; Manoharan R; Deinum G; Itzkan I; Dasari RR; Feld MS Detection and identification of a single DNA base molecule using surface-enhanced Raman scattering (SERS). Phys. Rev. E 1998, 57, R6281–R6284.

(13). Chen C; Li Y; Kerman S; Neutens P; Willems K; Cornelissen S; Lagae L; Stakenborg T; Dorpe PV High spatial resolution nanoslit SERS for single-molecule nucleobase sensing. Nature Communications 2018, 9, 1733.

(14). Maker P; Terhune R Study of optical effects due to an induced polarization third order in the electric field strength. Physical Review 1965, 137, A801.

(15). Evans CL; Xie XS Coherent anti-Stokes Raman scattering microscopy: chemical imaging for biology and medicine. Annu. Rev. Anal. Chem 2008, 1, 883–909.

(16). Cheng J-X; Xie X Coherent anti-Stokes Raman scattering microscopy: instrumentation, theory, and application. J. Phys. Chem. B 2004, 108, 827–840.

(17). Cui M; Bachler BR; Ogilvie JP Comparing coherent and spontaneous Raman scattering under biological imaging conditions. Optics letters 2009, 34, 773–775. [PubMed: 19282928]

(18). Potma EO; Evans CL; Xie XS Heterodyne coherent anti-Stokes Raman scattering (CARS) imaging. Optics letters 2006, 31, 241–243. [PubMed: 16441043]

(19). Zumbusch A; Holtom GR; Xie XS Three-dimensional vibrational imaging by coherent anti-Stokes Raman scattering. Physical review letters 1999, 82, 4142.

(20). Ideguchi T; Holzner S; Bernhardt B; Guelachvili G; Picqué N; Hänsch TW Coherent Raman spectro-imaging with laser frequency combs. Nature 2013, 502, 355–358. [PubMed: 24132293]

(21). Kameyama R; Takizawa S; Hiramatsu K; Goda K Dual-Comb Coherent Raman Spectroscopy with near 100% Duty Cycle. ACS Photonics 2021, 8, 975–981.

(22). Zhang C; Huang K-C; Rajwa B; Li J; Yang S; Lin H; sheng Liao C; Eakins G; Kuang S; Patsekin V et al. Stimulated Raman scattering flow cytometry for label-free single-particle analysis. Optica 2017, 4, 103–109. [PubMed: 39238893]

(23). Chen CK; de Castro ARB; Shen YR; DeMartini F Surface Coherent Anti-Stokes Raman Spectroscopy. Phys. Rev. Lett 1979, 43, 946–949.

(24). Koo T-W; Chan S; Berlin AA Single-molecule detection of biomolecules by surface-enhanced coherent anti-Stokes Raman scattering. Optics letters 2005, 30, 1024–1026. [PubMed: 15906991]

(25). Yampolsky S; Fishman DA; Dey S; Hulkko E; Banik M; Potma EO; Apkarian VA Seeing a single molecule vibrate through time-resolved coherent anti-Stokes Raman scattering. Nature Photonics 2014, 8, 650–656.

(26). Zhang Y; Zhen Y-R; Neumann O; Day JK; Nordlander P; Halas NJ Coherent anti-Stokes Raman scattering with single-molecule sensitivity using a plasmonic Fano resonance. Nature communications 2014, 5, 1–7.

(27). Zong C; Cheng R; Chen F; Lin P; Zhang M; Chen Z; Li C; Yang C; Cheng J-X Wide-Field Surface-Enhanced Coherent Anti-Stokes Raman Scattering Microscopy. ACS Photonics 2022, 9, 1042–1049.

(28). Sun C-K; Vallée F; Acioli L; Ippen E; Fujimoto J Femtosecond investigation of electron thermalization in gold. Physical Review B 1993, 48, 12365.

(29). Groeneveld RH; Sprik R; Lagendijk A Femtosecond spectroscopy of electron-electron and electron-phonon energy relaxation in Ag and Au. Physical Review B 1995, 51, 11433.

(30). Elsayed-Ali H; Juhasz T; Smith G; Bron W Femtosecond thermoreflectivity and thermotransmissivity of polycrystalline and single-crystalline gold films. Physical Review B 1991, 43, 4488.

(31). Bouhelier A; Bachelot R; Lerondel G; Kostcheev S; Royer P; Wiederrecht G Surface plasmon characteristics of tunable photoluminescence in single gold nanorods. Physical review letters 2005, 95, 267405. [PubMed: 16486405]

(32). Li X; Xiao D; Zhang Z Landau damping of quantum plasmons in metal nanostructures. New Journal of Physics 2013, 15, 023011.

(33). Brongersma ML; Halas NJ; Nordlander P Plasmon-induced hot carrier science and technology. Nature nanotechnology 2015, 10, 25–34.

(34). Alabastri A; Toma A; Malerba M; De Angelis F; Proietti Zaccaria R High temperature nanoplasmonics: the key role of nonlinear effects. ACS Photonics 2015, 2, 115–120.

(35). Dey S; Banik M; Hulkko E; Rodriguez K; Apkarian V; Galperin M; Nitzan A Observation and analysis of Fano-like lineshapes in the Raman spectra of molecules adsorbed at metal interfaces. Physical Review B 2016, 93, 035411.

(36). Crampton KT; Fast A; Potma EO; Apkarian VA Junction plasmon driven population inversion of molecular vibrations: a picosecond surface-enhanced Raman spectroscopy study. Nano letters 2018, 18, 5791–5796. [PubMed: 30064221]

(37). Crampton KT; Zeytunyan A; Fast AS; Ladani FT; Alfonso-Garcia A; Banik M; Yampolsky S; Fishman DA; Potma EO; Apkarian VA Ultrafast coherent Raman scattering at plasmonic nanojunctions. The Journal of Physical Chemistry C 2016, 120, 20943–20953.

(38). Keldysh L, et al. Ionization in the field of a strong electromagnetic wave. Sov. Phys. JETP 1965, 20, 1307–1314.

(39). Fast A; Kenison JP; Syme CD; Potma EO Surface-enhanced coherent anti-Stokes Raman imaging of lipids. Applied optics 2016, 55, 5994–6000. [PubMed: 27505381]

(40). Kenison JP; Fast A; Guo F; LeBon A; Jiang W; Potma EO Imaging properties of surface-enhanced coherent anti-Stokes Raman scattering microscopy on thin gold films. JOSA B 2017, 34, 2104–2114.

(41). Lévêque G; Martin OJ Optical interactions in a plasmonic particle coupled to a metallic film. Optics express 2006, 14, 9971–9981. [PubMed: 19529391]

(42). Nordlander P; Le F Plasmonic structure and electromagnetic field enhancements in the metallic nanoparticle-film system. Applied Physics B 2006, 84, 35–41.

(43). Benz F; Chikkaraddy R; Salmon A; Ohadi H; De Nijs B; Mertens J; Carnegie C; Bowman RW; Baumberg JJ SERS of individual nanoparticles on a mirror: size does matter, but so does shape. The journal of physical chemistry letters 2016, 7, 2264–2269. [PubMed: 27223478]

(44). Bontempi N; Vassalini I; Danesi S; Ferroni M; Donarelli M; Colombi P; Alessandri I Non-plasmonic SERS with silicon: is it really safe? new insights into the optothermal properties of core/shell microbeads. The journal of physical chemistry letters 2018, 9, 2127–2132. [PubMed: 29601206]

(45). Baumberg JJ; Aizpurua J; Mikkelsen MH; Smith DR Extreme nanophotonics from ultrathin metallic gaps. Nature materials 2019, 18, 668–678. [PubMed: 30936482]

(46). Caldarola M; Albella P; Cortés E; Rahmani M; Roschuk T; Grinblat G; Oulton RF; Bragas AV; Maier SA Non-plasmonic nanoantennas for surface enhanced spectroscopies with ultra-low heat conversion. Nature communications 2015, 6, 1–8.

(47). Albella P; Alcaraz de la Osa R; Moreno F; Maier SA Electric and magnetic field enhancement with ultralow heat radiation dielectric nanoantennas: considerations for surface-enhanced spectroscopies. Acs Photonics 2014, 1, 524–529.

(48). Novotny L; Hecht B Principles of nano-optics; Cambridge university press, 2012.

(49). Albella P; Poyli MA; Schmidt MK; Maier SA; Moreno F; Sáenz JJ; Aizpurua J Low-loss electric and magnetic field-enhanced spectroscopy with subwavelength silicon dimers. The Journal of Physical Chemistry C 2013, 117, 13573–13584.

(50). Edward DP; Palik I Handbook of optical constants of solids. 1985.

(51). Abedin S; Kenison J; Vargas C; Potma EO Sensing biomolecular interactions by the luminescence of a planar gold film. Analytical Chemistry 2019, 91, 15883–15889. [PubMed: 31755696]

(52). Boyd GT; Yu ZH; Shen YR Photoinduced luminescence from the noble metals and its enhancement on roughened surfaces. Phys. Rev. B 1986, 33, 7923–7936.

(53). Gui JY; Stern DA; Frank DG; Lu F; Zapien DC; Hubbard AT Adsorption and surface structural chemistry of thiophenol, benzyl mercaptan, and alkyl mercaptans. Comparative studies at silver (111) and platinum (111) electrodes by means of Auger spectroscopy, electron energy loss spectroscopy, low energy electron diffraction and electrochemistry. Langmuir 1991, 7, 955–963.

(54). McFarland AD; Young MA; Dieringer JA; Van Duyne RP Wavelength-scanned surface-enhanced Raman excitation spectroscopy. The Journal of Physical Chemistry B 2005, 109, 11279–11285. [PubMed: 16852377]

(55). Wan L-J; Terashima M; Noda H; Osawa M Molecular orientation and ordered structure of benzenethiol adsorbed on gold (111). The Journal of Physical Chemistry B 2000, 104, 3563–3569.

(56). Canamares MV; Chenal C; Birke RL; Lombardi JR DFT, SERS, and single-molecule SERS of crystal violet. The Journal of Physical Chemistry C 2008, 112, 20295–20300.
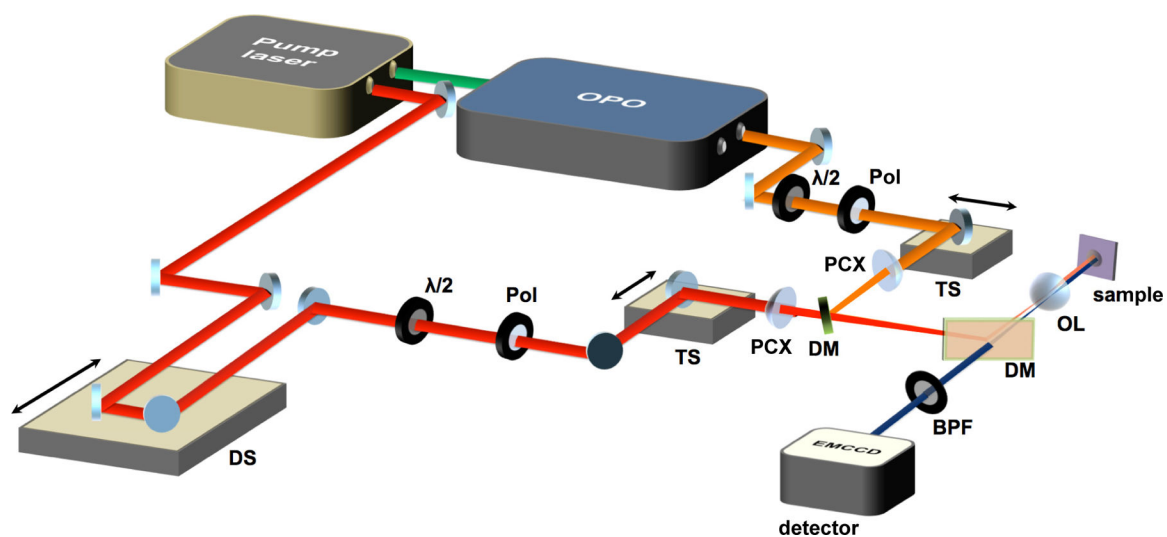
Figure 1:
Schematic of the wide-field SE-CARS microscope system. DS, delay stage; $\lambda/2$, half-wave plate; Pol, linear polarizer; TS, translation stage; PCX, plano-convex lens; DM, dichroic mirror; OL, 1.49 NA objective lens; BPF, bandpass filter.
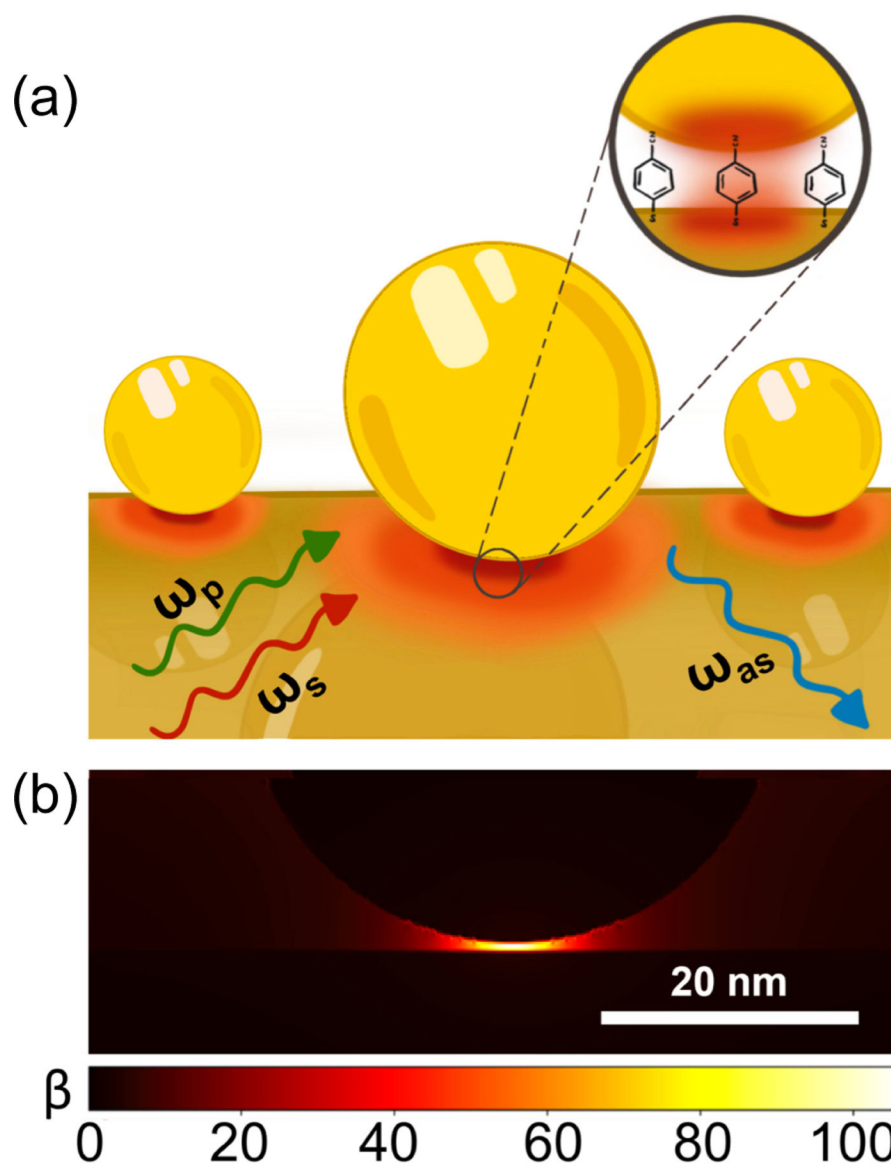
Figure 2:
(a) Schematic of experimental geometry for SE-CARS at Au film-Au particle nanojunctions.
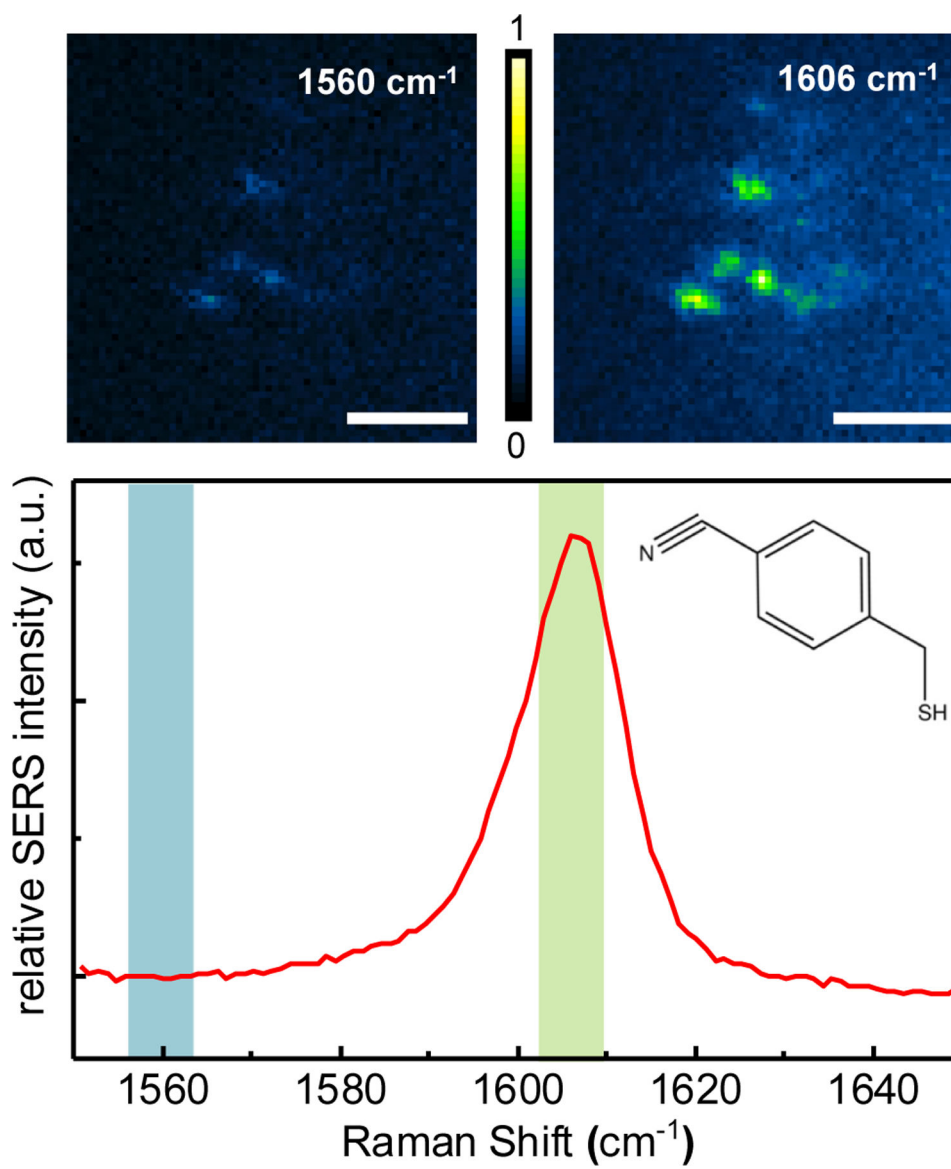(b) FDTD simulation near the junction under 909 nm illumination in the Kretschmann
configuration.

Figure 3:
SE-CARS images of MMBN molecules located in a Au film-Au particle nanojunction. On-resonance images were taken at 1606 cm^{-1} and off-resonance images were taken at 1560 cm^{-1}, as shown in the SERS spectrum of MMBN immobilized on a 40 nm gold nanoparticle. Scale bar is 2 μm.
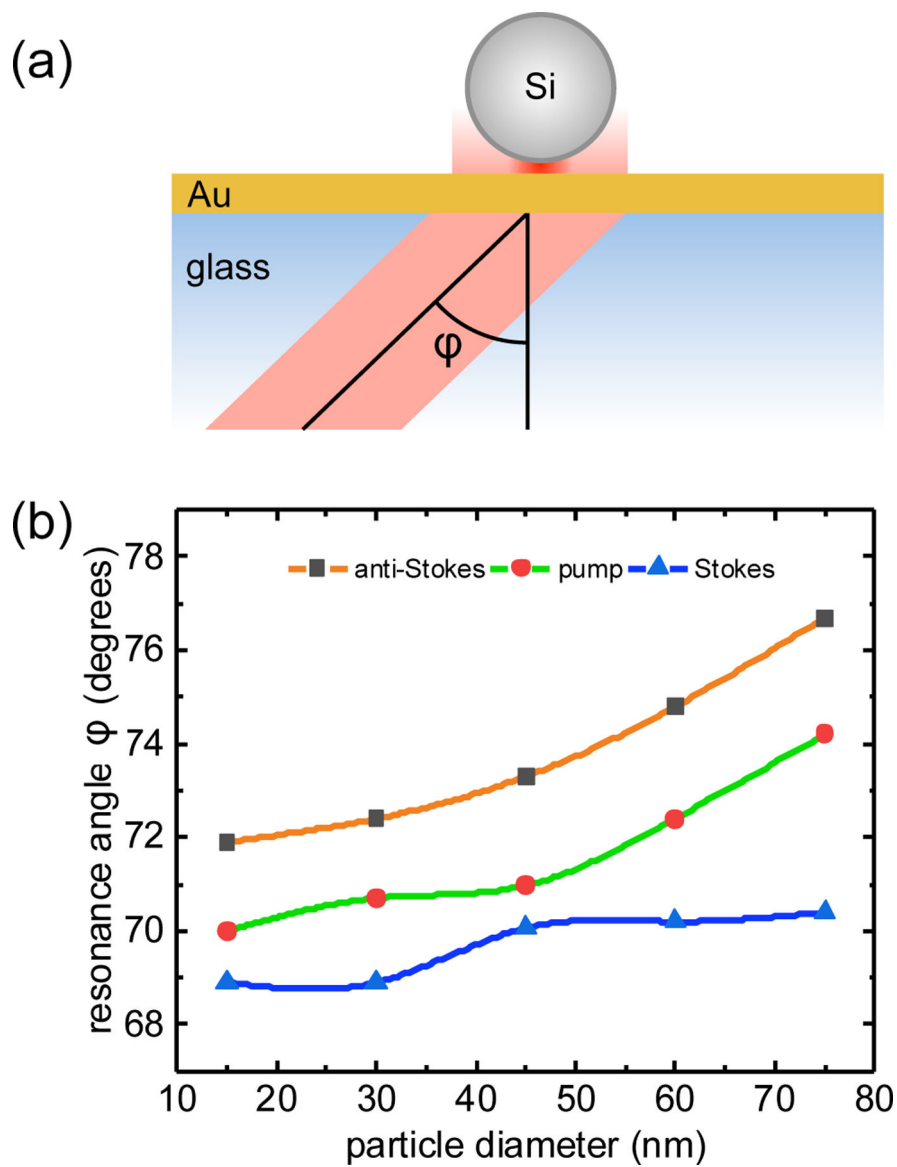
Figure 4:
a) Cartoon of the incoming beam arriving at the Kretschmann angle (φ) at the Au film-Si particle hereojunction b) Kretschmann angles for pump, Stokes and anti-Stokes wavelengths for different diameters of silicon nanoparticles. The lines connecting the data points are used here as visual guides only. No fitting is performed on these data
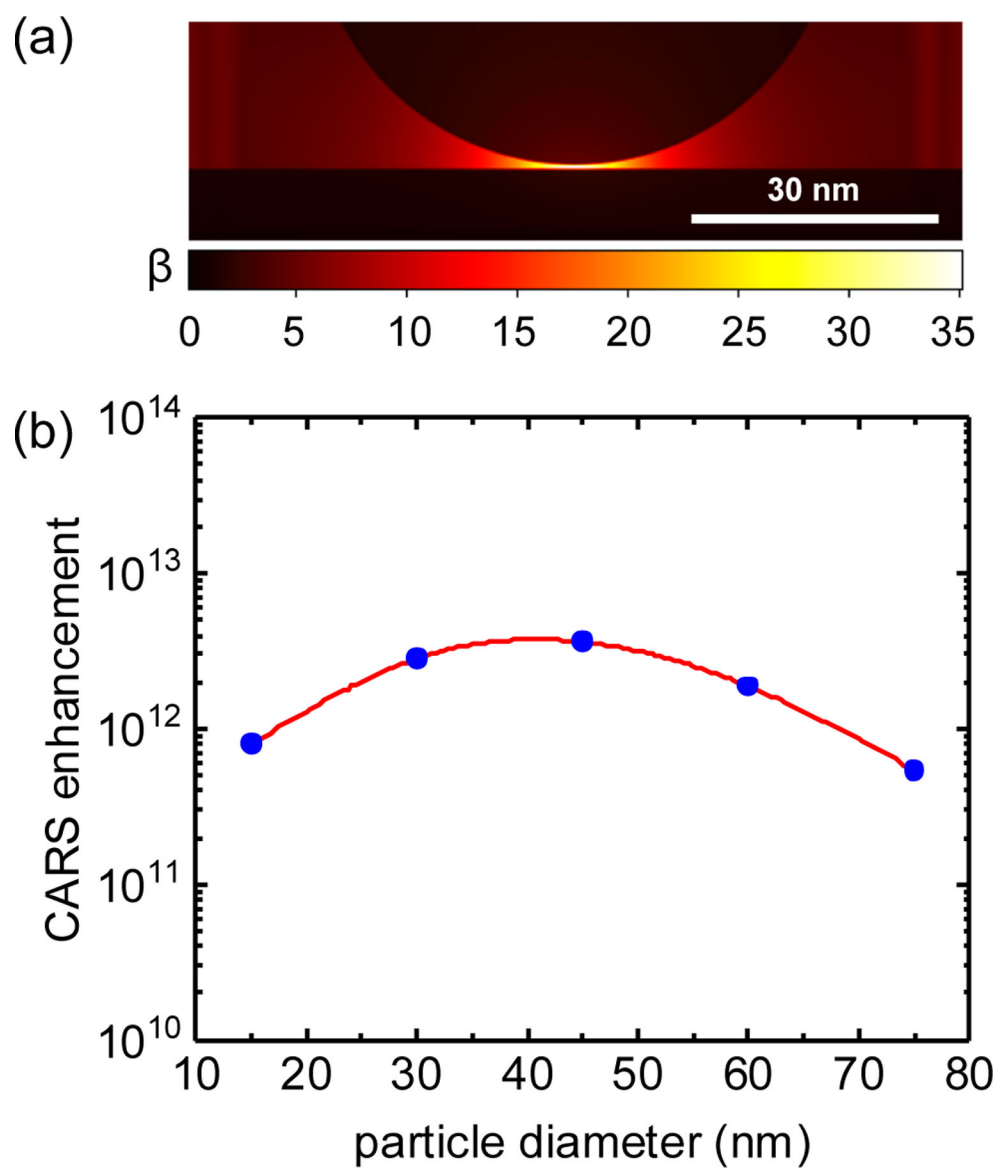
Figure 5:
a) FDTD calculations for locally enhanced fields near the Au film-Si particle heterojunction at the pump wavelength of 909 nm. Particle has a diameter of 60 nm. b) Overall SE-CARS enhancement $((\beta_p^4 \beta_s^2 \beta_{as}^2))$ factor as a function of Si nanoparticle diameter
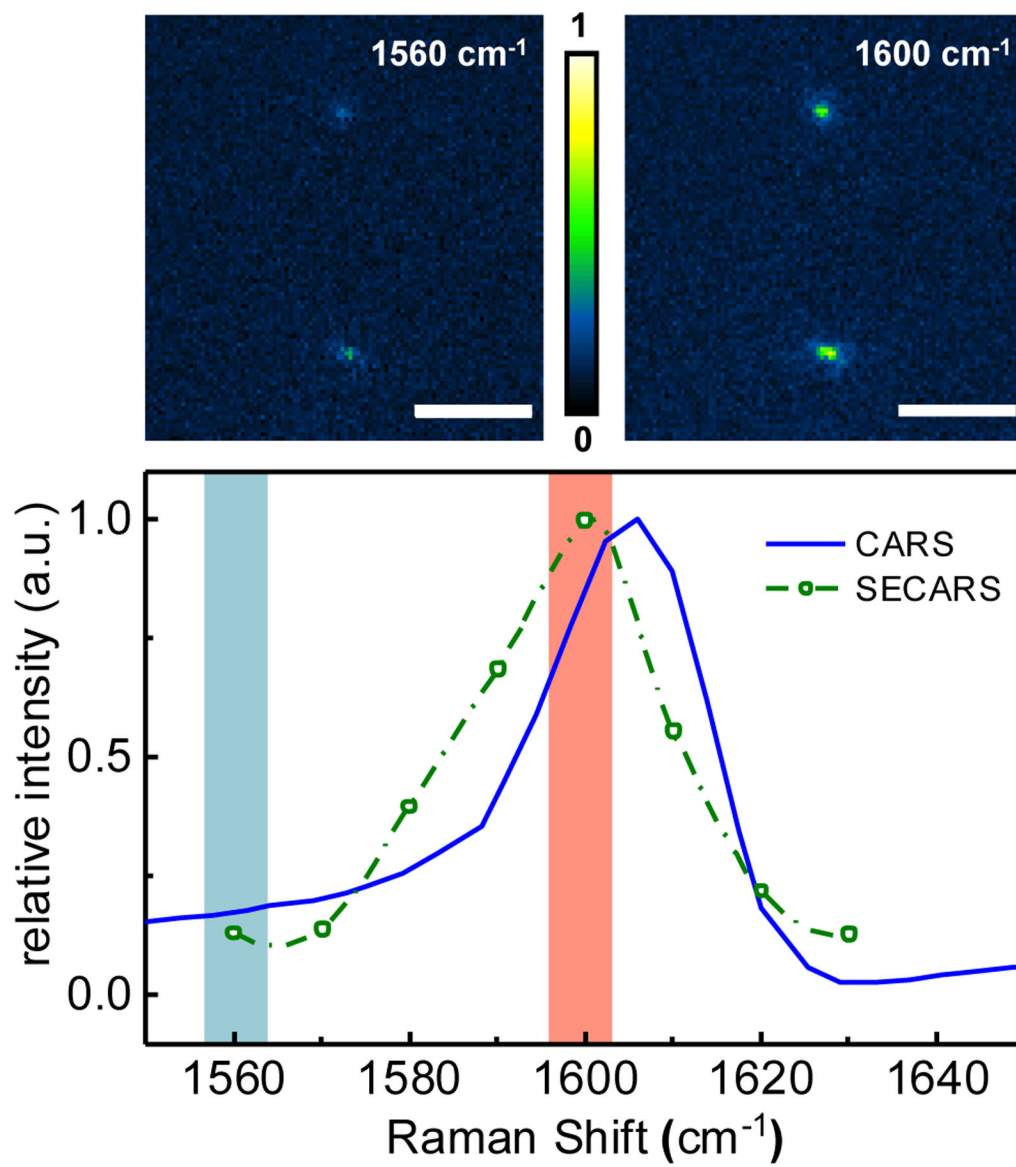
Figure 6:
SE-CARS spectrum of MMBN located inside Au film-Si particle heterojunction. The green dots show SE-CARS data points taken at 10 cm^{-1} intervals. The CARS spectrum of bulk MMBN is shown as the blue trace as reference. Above the spectrum, representative on and off-resonance images are shown. Scale bar is 5 μm.